



**HAL**  
open science

## Cross-comparison of global simulation models applied to Mercury's dayside magnetosphere

Sae Aizawa, Léa Griton, Jorge Amaya, Nicolas André, Jan Deca, Willi Exner, Shahab Fatemi, Vincent Génot, Daniel Heyner, Go Murakami, et al.

### ► To cite this version:

Sae Aizawa, Léa Griton, Jorge Amaya, Nicolas André, Jan Deca, et al.. Cross-comparison of global simulation models applied to Mercury's dayside magnetosphere. 2020. hal-02551111v1

**HAL Id: hal-02551111**

**<https://hal.science/hal-02551111v1>**

Preprint submitted on 22 Apr 2020 (v1), last revised 2 Feb 2021 (v3)

**HAL** is a multi-disciplinary open access archive for the deposit and dissemination of scientific research documents, whether they are published or not. The documents may come from teaching and research institutions in France or abroad, or from public or private research centers.

L'archive ouverte pluridisciplinaire **HAL**, est destinée au dépôt et à la diffusion de documents scientifiques de niveau recherche, publiés ou non, émanant des établissements d'enseignement et de recherche français ou étrangers, des laboratoires publics ou privés.

# Cross-comparison of global simulation models applied to Mercury's dayside magnetosphere

S. Aizawa<sup>1,2</sup>, L. S. Griton<sup>1,12</sup>, J. Amaya<sup>3</sup>, N. André<sup>1</sup>, J. Deca<sup>4,5,6</sup>, W.  
Exner<sup>7,8,9</sup>, S. Fatemi<sup>10,17</sup>, V. Génot<sup>1</sup>, D. Heyner<sup>7</sup>, G. Murakami<sup>11</sup>, F.  
Pantellini<sup>12</sup>, H. Usui<sup>13</sup>, M. Yagi<sup>14</sup>, L. Beigbeder<sup>15</sup>, M. Gangloff<sup>1</sup>, M.  
Bouchemit<sup>1</sup>, and E. Budnik<sup>16</sup>

<sup>1</sup>IRAP, CNRS-CNES-UPS, Toulouse, France

<sup>2</sup>Graduate School of Science, Tohoku University, Sendai, Japan

<sup>3</sup>CmPA, Mathematics Department, KU Leuven, Belgium

<sup>4</sup>Laboratory for Atmospheric and Space Physics (LASP), University of Colorado Boulder, Boulder,  
Colorado 80303, USA

<sup>5</sup>Institute for Modeling Plasma, Atmospheres and Cosmic Dust, NASA/SSERVI, California 94035, USA

<sup>6</sup>Laboratoire Atmosphères, Milieux, Observations Spatiales (LATMOS), Université de Versailles à Saint  
Quentin, 78280 Guyancourt, France

<sup>7</sup>Institute for Geophysics and extraterrestrial Physics, Technische Universität Braunschweig,  
Braunschweig, Germany

<sup>8</sup>Institute for Theoretical Physics, Technische Universität Braunschweig, Braunschweig, Germany

<sup>9</sup>School of Earth and Atmospheric Sciences, Georgia Institute of Technology, Atlanta, USA

<sup>10</sup>Swedish Institute of Space Physics, Kiruna, Sweden

<sup>11</sup>ISAS/JAXA, Sagami-hara, Japan

<sup>12</sup>LESIA, Observatoire de Paris, Université PSL, CNRS, Sorbonne Université, Université de Paris, 5 place

Jules Janssen, 92195 Meudon, France

<sup>13</sup>Kobe University, Kobe, Japan

<sup>14</sup>RIKEN, Kobe, Japan

<sup>15</sup>GFI, Toulouse, France

<sup>16</sup>Noveltis, Toulouse, France

<sup>17</sup>Department of Physics at Umeå University, Umeå, Sweden

## Key Points:

- 
- First comparison of multiple global simulations of the solar wind interaction with Mercury's dayside magnetosphere
- The results of four distinct simulation approaches are juxtaposed with MESSENGER observations
- In contrast to the magnetosheath thickness, the location of the simulated bow shock depends on the inner boundary condition of the model

## Abstract

We present the first comparison of multiple global simulations of the solar wind interaction with Mercury’s dayside magnetosphere, conducted in function of the international collaborative project SHOTS - Studies on Hermean magnetosphere Oriented Theories and Simulations. Two magnetohydrodynamic and two hybrid (ion kinetic, electron fluid) simulation codes are used to investigate a scenario with a northward orientation of the interplanetary magnetic field. We juxtapose the results of the four codes for a theoretical case and a MESSENGER orbit with similar upstream plasma conditions. The different models agree on a bow shock and magnetopause location at  $2.1 R_M$  and  $1.4 R_M$ , respectively. It is found that the location of the simulated bow shock depends on the inner boundary condition of the model. To assess and characterize the different features of each code, the thickness of the magnetosheath has been compared as well. The four models are also used for the comparison with MESSENGER observations, and virtual sampling of Mio and MPO spacecraft of BepiColombo mission. Our ability to more accurately predict the structure of the Hermean magnetosphere will aid the analysis of BepiColombo’s plasma measurements.

## 1 Introduction

Mercury is a planet of extremes that is continuously battered by a harsh and dynamic solar wind. The planet’s eccentric orbit crosses regions where nearly 40% of the thermal pressure is carried by alpha particles and heavy ions during fast solar wind phases (Gershman et al., 2012). Combined with a highly variable slow solar wind component that includes interplanetary magnetic field magnitudes up to 30 nT and a small Parker spiral angle, Mercury’s weak internal magnetic field produces a unique magnetosphere in the solar system (Korth et al., 2018; Slavin et al., 2018). In particular, the significant offset between the magnetic dipole origin and the center of the planet results in a surface magnetic field strength in the northern hemisphere that is double the nominal value estimated for the southern hemisphere. The estimated distance between the sub-solar magnetopause and the surface is only half of the planetary radius, meaning that often the solar wind can directly interact with the surface, even outside the magnetospheric cusps. Mercury’s magnetosphere is a factor of 20 smaller than Earth’s magnetosphere. Because Mercury takes up a significant volume within its magnetosphere, particle precipitation patterns and differential space weathering are as variable as the upstream solar wind (Kallio et al., 2008; Raines et al., 2014). The absence of a significant ionosphere makes Mercury’s conductive core an integral part of the electrodynamic current closure and complicates the evolution of the complex local plasma environment even more (Johnson et al., 2016).

Numerical simulations of the solar wind interaction with the Hermean magnetosphere have thus far adopted multi-fluid/magnetohydrodynamic (e.g., Kabin et al. (2000); Benna et al. (2010); Jia et al. (2015); Dong et al. (2019)) and hybrid approaches (treating the electron populations as a (massless) fluid; e.g., Kallio and Janhunen (2003); P. Trávníček et al. (2007); P. M. Trávníček et al. (2010); Wang et al. (2010)). These models, designed to focus on the ion kinetics, have been successful in recreating the general structure of Mercury’s local plasma environment. For example, with a hybrid model Müller et al. (2012) characterised a diamagnetic current system that originates from the proton pressure gradients at Mercury’s inner magnetosphere to explain the day- and night-side diamagnetic decreases observed by MESSENGER (Slavin et al., 2008; Anderson et al., 2011). In addition, recent numerical developments have produced the first fully kinetic, global simulations of the Hermean magnetosphere (Peng, Markidis, Laure, et al., 2015; Peng, Markidis, Vaivads, et al., 2015; Chen et al., 2019).

Both Mariner-10 and MESSENGER have shown that including finite-gyroradius effects and electron dynamics are insurmountable to fully understand the Hermean plasma

environment (Slavin et al., 2018). The BepiColombo plasma instruments, complementary to the previous missions, will focus on direct measurements of the response of Mercury’s magnetosphere and its near-space environment to dynamic changes in the solar wind, including plasma-wave-charged-particle resonances, kinetic-scale instabilities and particle distributions, and energy transfer via field-aligned currents and waves (Slavin et al., 2018). In order to optimally prepare for the measurement campaign and to be able to fully interpret and analyse the data, or in other words, to exploit most efficiently the multi-point measurements allowed by the dual spacecraft and the synergies between the various sensors of the on-board plasma suite, sophisticated modelling tools are required.

The SHOTS (Studies on Hermean magnetosphere Oriented Theories and Simulations) project<sup>(1)</sup> has been established as an integral part of the BepiColombo Young Scientist Working Group<sup>(2)</sup>. Its aim is to share and compare simulations results among the BepiColombo Science Working Team to prepare the scientific analysis of the in situ observations gathered by the Mercury Magnetospheric Orbiter (MIO; Mukai et al. (2006)) and Mercury Planetary Orbiter (MPO; Milillo et al. (2010)).

In this first comparative study, we identify the differences of a fluid and hybrid simulation approach to model the structure of the Hermean magnetosphere and its plasma environment. Also, we compare the bow shock and magnetopause locations with a representative set of MESSENGER measurements.

## 2 Model description

The four computer models used in this comparison study are briefly described here. Two magnetohydrodynamic (MHD) and two hybrid codes have been employed to identify the consequences of the different assumptions that are implemented in the physical model of the codes.

The MPI-AMRVAC code (hereafter AMRVAC) is a three-dimensional non-relativistic MHD code, previously used, e.g., to investigate the interaction of the solar wind with a planetary environment (Keppens et al., 2012). AMRVAC integrates the MHD equations using a two-step Lax-Friedrichs-type scheme (TVDFL) associated with a Woodward gradient limiter. A Powell correction is also used to satisfy the  $\nabla \cdot \mathbf{B} = 0$  condition at each time step (Powell et al., 1999). In order to limit magnetic diffusion, the magnetic field  $\mathbf{B}$  is split into an analytically prescribed background field  $\mathbf{B}_0$  and a residual field  $\mathbf{B}_1$  (Griton et al., 2018). The full system of equations is solved on a spherical grid that is linearly spaced along the angular coordinates  $\theta$  and  $\phi$  and logarithmically spaced along the radial coordinate  $r$ . Hence, the simulation domain itself is a spherical shell. At the outer boundary, free slip conditions  $\partial/\partial r = 0$  are applied to all fields where the angle between the solar wind direction and the normal to the boundary direction is  $< 80^\circ$ . Ambient (upstream) solar wind conditions are set at the remaining sides of the domain. At the inner boundary of the simulation domain, here the planetary surface, the radial velocity is set to zero. A free slip condition is applied to the tangential components of the momentum  $\rho \mathbf{u}$ . If the radial velocity immediately above the surface is positive (i.e. in case of outflow), the plasma number density and the total fluid pressure are set to  $n_p = n_e = 15 \text{ cm}^{-3}$  and  $p = 0.1 \text{ nPa}$ , respectively. On the other hand, if the radial velocity immediately above the surface is negative (i.e. in case of inflow)  $n_p$  and  $p$  are allowed to float within the range  $[15, 150] \text{ cm}^{-3}$  and  $[0.1, 1] \text{ nPa}$ . A free slip condition is also applied to the normal component of  $\mathbf{B}_1$  at the surface. The tangential components are set to zero.

<sup>1</sup> <http://shots-bepicolombo.irap.omp.eu>

<sup>2</sup> <https://sites.google.com/view/bepi-ys-wg-workshop>

133 YAGI's code is the second three-dimensional MHD model we use (Yagi et al., 2009,  
 134 2010). In contrast to AMRVAC, a uniform Cartesian grid is adopted and the vector po-  
 135 tential  $\mathbf{A}$  is computed instead of the magnetic field, ensuring  $\nabla \cdot \mathbf{B} = 0$  by definition.  
 136 In addition, a Rational-CIP algorithm is implemented to solve the advection term. A  
 137 fourth-order Runge Kutta and a fourth-order central difference method are used to solve  
 138 the non-advection terms needed to advance the numerical scheme in time and space, re-  
 139 spectively. The inner boundary of the computational domain is the planetary surface and  
 140 Mercury is treated as a reflective obstacle, allowing no flux to penetrate across the sur-  
 141 face. We also do not allow any radial pressure and density gradient at the planetary sur-  
 142 face. These conditions accommodate a smooth convection of the dipole magnetic field  
 143 in the vicinity of the planet, mimicking a conducting obstacle.

144 AIKEF (Adaptive Ion Kinetic Electron Fluid) is a hybrid code that operates on  
 145 a Cartesian grid. The mesh automatically adapts its resolution in regions where large  
 146 field gradients exist (Müller et al., 2011). Contrary to MHD, a hybrid model treats ions  
 147 kinetically and uses computational particles to represent their velocity distribution. Elec-  
 148 trons are included as a massless charge-neutralizing fluid. To include induction effects,  
 149 a radial resistivity profile is applied. The maximum resistivity is set to  $1.21 \times 10^7$  [Ohm  
 150 m] within the mantle. The profile at the core-mantle boundary and the surface are adopted  
 151 from Jia et al. (2015). Mercury's surface is treated as a perfect plasma absorber, i.e., par-  
 152 ticles impacting the surface are removed. Within the vacuum regions of the nightside  
 153 magnetosphere, ghost-particles with the same charge-to-mass ratio as the upstream solar  
 154 wind protons are inserted to allow local magnetic field diffusion. Their density is ten-  
 155 uous so that no physical feedback onto the dynamics of the magnetosphere is present.  
 156 The model has previously been applied to Mercury's magnetosphere (Müller et al., 2012;  
 157 Exner et al., 2018).

158 The Amitis (advanced modeling infrastructure in space simulations) is a GPU-based  
 159 (Graphics Processing Units) three-dimensional hybrid model of plasma that currently  
 160 runs only on a single CPU-GPU pair. It has been developed to reduce the computational  
 161 resources that are typically needed for running global simulations and resulted in per-  
 162 formance enhancement of 10x-100x over its CPU-based predecessor (Fatemi et al., 2017).  
 163 The model kinetically tracks individual positively charged particles (ions) by solving the  
 164 Lorentz equation of motion while using a fluid description for mass-less electrons. The  
 165 electric field,  $\mathbf{E}$ , is directly calculated from the electron momentum equation and Fara-  
 166 day's law,  $\partial \mathbf{B} / \partial t = -\nabla \times \mathbf{E}$ , is used to advance the magnetic field,  $\mathbf{B}$ , in time. The  
 167 model is grid-based and uses regular-spaced, cell-center Cartesian grids to solve all the  
 168 equations. The model self-consistently couples the geophysical, induced electromagnetic  
 169 response of the interior of a planetary body to the electromagnetic response of the in-  
 170 cident plasma and magnetic fields by solving Maxwell's equations for plasma and mag-  
 171 netic diffusion equation ( $\partial \mathbf{B} / \partial t = -\nabla \times \nabla \times \mathbf{B} / \mu_0 \sigma$ ) for the interior of an object, where  
 172  $\mu_0$  is the permeability of free space and  $\sigma$  is the conductive profile for the interior of a  
 173 planetary body (for more details, see Fatemi et al. (2017)). The model allows real-time  
 174 simulations and it has been extensively applied to study plasma interaction with the Moon,  
 175 asteroid 16 Psyche, and Mercury and validated against observations by ARTEMIS and  
 176 MESSENGER (Fatemi et al., 2017; Fatemi et al., 2018; Fatemi & Poppe, 2018; Fuqua Hav-  
 177 iland et al., 2019; Garrick-Bethell et al., 2019; Poppe, 2019). In Amitis, when a parti-  
 178 cle impacts the surface of an object, the particle is removed from the simulation domain,  
 179 and when a vacuum region forms behind an object, which is due to the plasma absorp-  
 180 tion upstream, the entire vacuum region is assumed to be resistive with resistivity  $10^7$   
 181 [ $\Omega \cdot \text{m}$ ]. The resistivity assumption in the vacuum is in contrast to AIKEF that fill in the  
 182 vacuum region with ghost particles. For our simulations presented here and obtained from  
 183 the Amitis code, both the particles and electromagnetic fields are assumed to be peri-  
 184 odic along the y and z axis in the MSO coordinate system. The solar wind flows along  
 185 the -x axis by continuously injecting solar wind ions at the most upstream grid cell. The

186 downstream boundary (the last grid cell along the -x axis), similar to the surface of a  
 187 planetary body, is a perfect plasma absorber.

**Table 1.** Summary of the numerical setting.

	Grid	Number of cell	Size of domain	Spatial Resolution
AMRVAC	Spherical	(36, 36, 72)	$r \in R_M [1, 10]$	213 x 161 km
YAGI	Cartesian	(Nx, Ny, Nz)	(, , )	122 km
AIKEF	Cartesian	(Nx, Ny, Nz)	(, , )	100 km
AMITIS	Cartesian	(Nx, Ny, Nz)	(, , )	170km

188 The other numerical settings, such as the number of cell, the size of simulation do-  
 189 main, and spatial resolution are summarized in Table 1. In details, because AMRVAC  
 190 has employed spherical coordinate system, a total number of cells is  $(N_r, N_\theta, N_\phi) = (36, 36, 72)$ ,  
 191 covering the radial interval  $r \in R_M [1, 10]$ . The horizontal and vertical cell size near  
 192 the surface are thus 213 km and 161 km, respectively. No mesh refinement is used here,  
 193 and output file is converted to the Uniform Cartesian grids. YAGI’s model performs on  
 194 the Cartesian grids with the uniform uniform spatial resolution of 122 km. In AIKEF,  
 195 macro particles are used, which exhibit the same charge-to-mass ratio  $q_i/m_i$  as the ion  
 196 species they are representing. In this study, the uniform Cartesian geometric is applied  
 197 with the spatial resolution of 100 km and the number of particle per cell is set to 25 to  
 198 accurately describe Maxwellian and non-Maxwellian distribution of different plasma species.  
 199 On the other hand, the number of particles per cell is 12 in AMITIS. The spatial res-  
 200 olution is now set to 170 km.

### 201 3 Methodology constraints

#### 202 3.1 Common visualization tools

203 We use netCDF as a multidimensional format with meta information for all simu-  
 204 lations. It allows us to have a unified format for comparative visualizations, data in-  
 205 teroperability and reusability. In the present study, we employ Paraview for 3D data vi-  
 206 sualization and analysis. In addition, we use 3Dview and AMDA, which makes use of  
 207 the SPASE simulation data model (Jacquey et al., 2010; Génot et al., 2010; Génot et al.,  
 208 2018; Roberts et al., 2018). Using SPICE kernels, 3Dview is a 3D JAVA tool that pro-  
 209 vides visualizations of the positions and attitudes of planetary missions and bodies in  
 210 combination with observational data, simulations, and analytical models. AMDA is an  
 211 online database and analysis tool in which in-situ observations, ground based observa-  
 212 tions, and models can be browsed, manipulated and downloaded (a workspace is avail-  
 213 able for each user). AMDA and 3Dview are developed by the CDPP (Centre de Données  
 214 de la Physique de Plasmas), and are now widely used by the space physics and plane-  
 215 tology communities and available to contributing developers under a GPLv3 licence.

#### 216 3.2 Common input parameters and simulation setup

217 In this work we discuss two cases: (a) a classical textbook case under purely north-  
 218 ward interplanetary magnetic field conditions, and (b) a direct comparison with a pre-  
 219 selected MESSENGER orbit. Using 4 different simulation frameworks inevitably leads  
 220 to a variety of numerical settings, such as boundary conditions, grid and spatial reso-  
 221 lutions, and the treatment of particles and electromagnetic fields at the planetary sur-  
 222 face. As a consequence, next to the physical model of each framework, also the numer-

223 ical treatment of the latter may influence the plasma behaviour in the simulated com-  
 224 putational domain.

225 All models work in the Mercury Solar Orbital (MSO) frame. The x-axis points to-  
 226 wards the Sun and the y-axis is chosen opposite to the orbital motion of Mercury. The  
 227 z-axis points to the geophysical north and completes the right-handed coordinate sys-  
 228 tem. The intrinsic magnetic field of the planet is set as an ideal dipole with a 480 km  
 229 offset towards the north from the planetary centre. The dipole moment is  $200 \text{ nT} \times R_M^3$ .  
 230 To avoid further numerical complexities, we do not include Mercury’s exosphere in our  
 231 simulations. An overview of all common input parameters is summarized in Table 2.

### 232 **3.2.1 Case a: Northward IMF**

233 Northward IMF conditions are chosen to ensure a most stable dayside magneto-  
 234 sphere structure. Typically, a southward IMF gives rise to unstable magnetosphere con-  
 235 ditions as the relatively short Dungey cycle at Mercury produces dayside magnetic re-  
 236 connection events in rapid succession, not allowing the system to relax in between (Slavin  
 237 et al., 2019).

238 The IMF magnitude is set to 20 nT and adopt a solar wind proton density of  $30 \text{ cm}^{-3}$ ,  
 239 Alfvén Mach number of 5, and a total plasma beta of 1.3. The solar wind speed mea-  
 240 sures  $400 \text{ km s}^{-1}$  (Sarantos et al., 2001; Winslow et al., 2013). In the MHD models the  
 241 density and temperatures are set using the sum of the respective proton and electron val-  
 242 ues (Table 2).

### 243 **3.2.2 Case b: MESSENGER comparison**

244 We select a MESSENGER orbit that allows a simulation setup as close as possi-  
 245 ble to our theoretical northward IMF case. Due to its mid-day to midnight orientation  
 246 (X-Z plane), orbit 1415 (November 8, 2012) allows for the easiest comparison. The or-  
 247 bit has a Disturbance Index less than 25, the lowest magnetic activity quartile; the z-  
 248 components of the IMF at the inbound and outbound bow shock crossings are positive  
 249 and within 2 nT of each other; and the IMF variability along the entire orbit is less than  
 250 10 nT, indicating stable solar wind conditions.

251 We use the inbound part of the orbit to compute an average IMF condition to be  
 252 inserted in our models. Further, the Alfvén Mach number is set to 5, the solar wind speed  
 253 equals  $459 \text{ km s}^{-1}$ , the proton and electron temperature measure 12 eV, and 18 eV, re-  
 254 spectively (Marsch et al., 1982; Wilson et al., 2018).

**Table 2.** Summary of the common input parameters. *SW* denote the solar wind.

	Northward case	MESSENGER case
Planetary radius $R_M$ [ $km$ ]	2440	2440
Planetary dipole moment [ $nT \times R_M^3$ ]	200	200
Northward dipole offset [ $km$ ]	480	480
SW proton density [ $cm^{-3}$ ]	30	40
SW proton + electron temperature [ $MK$ ]	0.25+0.25	0.14+0.21
SW total plasma $\beta$	1.3	0.69
SW Alfvén Mach number	5	5
SW plasma velocity [ $km s^{-1}$ ]	400	459
SW Sonic Mach number	6.8	8.5
IMF (X,Y,Z) components [ $nT$ ]	(0, 0, +20)	(25.28,-6,4.92)

## 4 Results

### 4.1 Purely northward IMF case

The purely northward IMF configuration gives the stable magnetosphere, thus, all simulation reaches the stationary state after the certain computational time ( 300 sec). Here the results from four different models have been compared to characterize each model. Figure 1 shows the density maps of solar wind proton in the  $X-Z$  plane on a logarithmic scale with the magnetic field lines. The two left panels show the results from MHD codes and the two right panels present the results from hybrid codes. It is clear that all models show a similar global structure of the Hermean magnetosphere, i.e., the shape of bow shock, high density in the magnetosheath, and the location of the cusp. However, the density population near the planet and inside the nightside magnetosphere, location of the magnetopause in the nightside look different among them.

Looking at each result, AMRVAC shows the less sharp shock structure at the bow shock, clear structure of the dayside magnetosphere with low density, some density concentration near the planet, and asymmetric magnetic field structure in the nightside magnetosphere which tends to the southward. Especially, the density concentration and southward tilting seem to be unique features of AMRVAC compared to others.

On the other hand, YAGI's code shows the sharper bow shock even though it is the same MHD model. The dayside magnetosphere can be identified by the structure of the magnetic field whereas it is filled with a higher density, which is almost the same or less as that in the magnetosheath. The structure of the magnetic field in the nightside is more symmetric or a little bit tilted to the northward, and there is no high density concentration.

The two panels on the right are the results from AIKEF and AMITIS. AIKEF also shows very sharp bowshock and the dayside magnetosphere can be identified also by the less dense plasma and the size of cusps seem to be narrow compared to that of MHDs. Because of no density concentration in the nightside, the cusp regions in the northern and southern hemispheres are easily identified in the density map. In the nightside, the magnetic field is slightly tilted to the north as YAGI's code does. Interestingly, AIKEF provides the curved magnetic field lines in the solar wind region. This is due to the smoothing effect in the code which can reduce the numerical instability. The right bottom panel represents the results from AMITIS. Because AMITIS does not employ any smoothing routine, the figure is busy compared to others. However, we see that the bowshock and magnetopause are clearly structured, and the solar wind plasma cannot penetrate into the dayside magnetosphere which is indicated by the lower density. The cusp structure



290 is similar to that of AIKEF, and the magnetic field configuration in the nightside is sym-  
 291 metric. Compared to other results, the density in the nightside seems to be low.

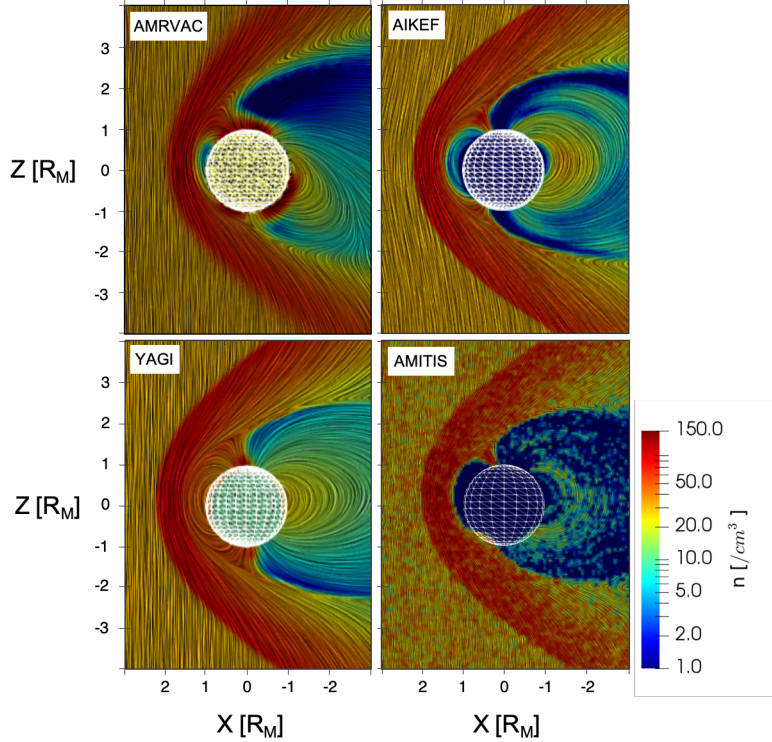


**Figure 1.** Density map in X-Z plane in log scale for 4 simulations. The panels on the left (right) are the results from MHD (hybrid) simulations. Length scales are normalized by Mercury radius.

292 In order to discuss the differences among them quantitatively, the pressure profile  
 293 along the subsolar line is shown in Figure 2. The dynamic and magnetic pressure is ex-  
 294 tracted and the locations of bowshock and magnetopause have been identified. The four  
 295 panels correspond to the four simulations. A solid line shows the dynamic pressure,  $\rho \mathbf{v}^2$ ,  
 296 while dashed line represents the magnetic pressure,  $B^2/2\mu$ . There is also a gray dot-dashed  
 297 line showing the magnetic pressure by the uncompressed dipole magnetic field to eval-  
 298 uate how much the planetary magnetic field is compressed by the solar wind. Please note  
 299 that the current setting of the intrinsic magnetic field is the same in all four simulations.  
 300 The gray vertical line at  $x = 1.12 R_M$ , showing the point where the dynamic pressure  
 301 and the uncompressed magnetic pressure as the reference magnetopause location. The  
 302 position of bow shock (BS) has been visually identified by the maximum gradient of ve-  
 303 locity and density (vertical solid red line), and the location of the magnetopause (MP)  
 304 has been identified by three ways, the one is the topology of the magnetic field line as  
 305 the farthest closed magnetic field line from the planet using Paraview, the other one is  
 306 the pressure equilibrium, and another is the current density. Because the MP location  
 307 identified by both the pressure equilibrium and the current density shows good agree-  
 308 ment, we take its value as a location of magnetopause indicated by the vertical dashed  
 309 red line in Figure 2.

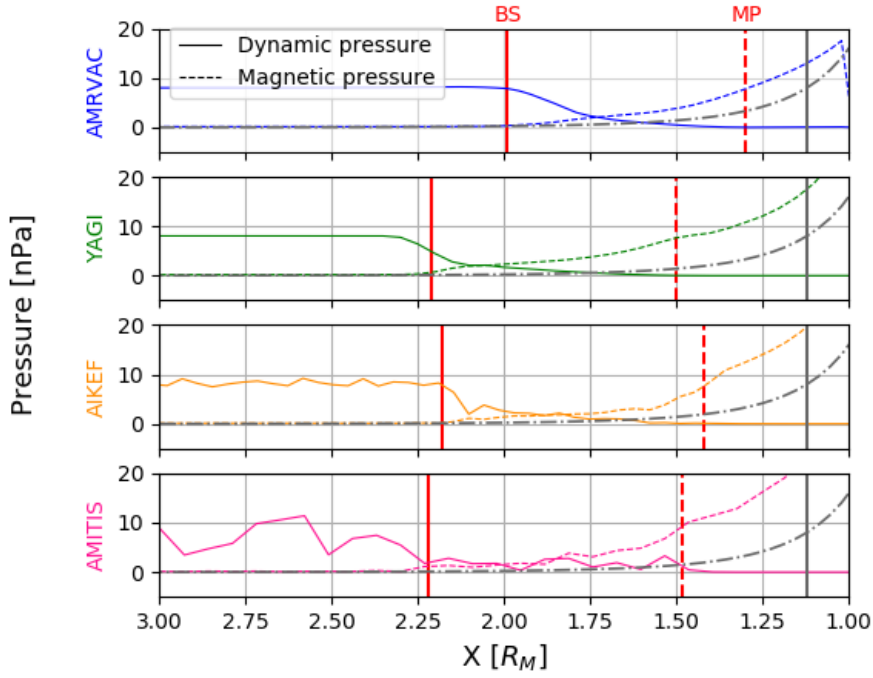


**Figure 2.** Dynamic (solid) and magnetic (dashed) pressure profiles along the X-axis (Sun-Mercury direction) from  $3 R_M$  to the planet surface on the day side, for the four simulation codes. The two MHD codes are on the top two panels and the hybrid ones in the two bottom panels. Positions of the bow-shock (BS) and magnetopause (MP) are shown with vertical red solid and dashed lines. The grey vertical line gives the theoretical expected position of the magnetopause.

310 In Figure 2, first of all, the locations of both bowshock and magnetopause vary slightly  
 311 among the models. The maximum difference for the bowshock is about  $0.23 R_M$  and  
 312 for the magnetopause is about  $0.2 R_M$ . The exact number of shock locations are sum-  
 313 marized in Table 2. The mean position of the magnetopause is  $1.425 R_M$ , and  $2.15 R_M$   
 314 for the bowshock. The standard deviation for the bowshock location is  $\sigma = 0.078$  with  
 315 the standard error of  $\pm 0.039$ , and  $\sigma = 0.094$  with the standard error of  $\pm 0.047$  for the  
 316 magnetopause location. According to Table 2, the location of the magnetopause varies  
 317 more than that of the bow shock, which can be understood due to the boundary con-  
 318 dition applied at the surface and inside of the planet. In order to compare those results  
 319 with minimum influence of numerical setting of the boundary condition, here we derive  
 320 the thickness of the magnetosheath as a key parameter. The mean value is  $0.725 R_M$   
 321 and its standard deviation  $\sigma$  is  $0.027$  with the standard error of  $\pm 0.019$ . Although the  
 322 results from hybrids seem to have the wider thickness, the error among four results is  
 323 small.

		BS [ $R_M$ ]	MP [ $R_M$ ]	Sheath thickness [ $R_M$ ]
MHD	AMRVAC	1.99	1.30	0.69
	YAGI	2.21	1.50	0.71
Hybrid	AIKEF	2.18	1.42	0.76
	AMITIS	2.22	1.48	0.74
Mean value		2.14	1.41	0.73
Standard Deviation $\sigma$		0.094	0.078	0.027
Standard Error $\sigma_{\bar{x}}$		$\pm 0.047$ ( $\pm 2.2\%$ )	$\pm 0.039$ ( $\pm 2.7\%$ )	$\pm 0.013$ ( $\pm 1.9\%$ )

**Table 3.** Summary of the bow shock and magnetopause locations, and the thickness of the magnetosheath for the four simulations (AMRVAC, YAGI’s code, AIKEF and AMITIS).

324 In addition to the shock location along the sub-solar line, here the reconnection site  
325 (so-called null point) around the cusp and location of the magnetopause in the night-  
326 side are also investigated as an important factor to determine the structure of the Her-  
327 mean magnetosphere. Figure 3 shows the  $X - Z$  map of the null points (indicated by  
328 colored circles) and locations of the magnetopause (represented by colored crosses) at  
329  $X = -2 R_M$  for each code. Two gray dashed lines represent the bowshock and magne-  
330 topause model (Slavin et al., 2009; Shue et al., 1997; Winslow et al., 2013) as references.  
331 The null point is normally identified by the high magnetic beta or very small magnitude  
332 of the magnetic field, or the topology of the magnetic field. In this study, because we have  
333 the simplest IMF configuration, the topology of the magnetic field showing the struc-  
334 ture of the magnetic reconnection is used for the identification using Paraview. It is clearly  
335 seen that the null points around the northern cusp are located more in the nightside and  
336 farther away from the planet while those around the southern cusp are near the termi-  
337 nator (except YAGI’s code) and close to the planet due to the offset of dipole field. Those  
338 reconnection sites are normally determined in each model depending on not only the phys-  
339 ical parameter we used such as the solar wind, dipole moment, but also the numerical  
340 parameters such as the resistivity, and they may play a big role to determine the loca-  
341 tion of shocks and the whole structure of the magnetosphere. For example, AMRVAC  
342 shows the largest asymmetry on the null point, and due to the rapid and continuous re-  
343 connection may make the titled southward structure of the magnetic field in the night-  
344 side and it may result in some high-density concentration near the surface. On the other  
345 hand, the locations of magnetopause in the nightside at  $X = -2 R_M$ , are obtained by  
346 the gradient of the density and current density. Except AMRVAC, other three models  
347 are located inside the referenced magnetopause model as we see in Figure 2. In partic-  
348 ular, the reference magnetopause model by Shue et al. (1997) with the parameters of  $R_{ss} =$   
349  $1.45 R_M$  and  $\alpha = 0.5$  is the best fit model for the MESSENGER observations. Con-  
350 sidering variations with this best fit model of the magnetopause, all four simulations show  
351 a good agreement with it even though our input IMF was purely northward. Northward  
352 IMF case shows that all models show very similar results in terms of the dayside mag-  
353 netosphere even different scale modelings.

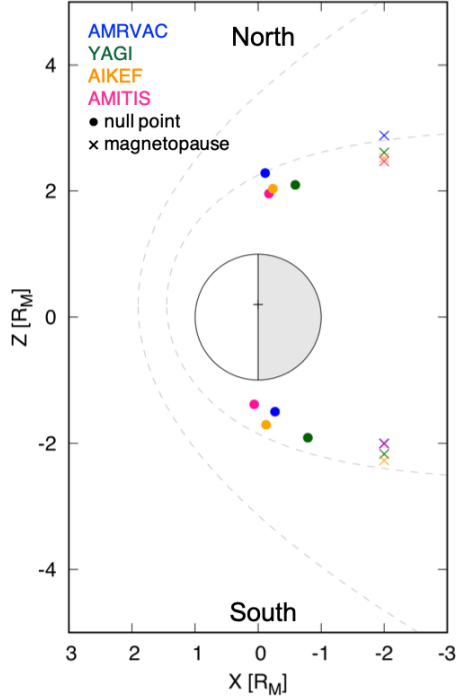


**Figure 3.** The locations of null points (colored circles) and magnetopause (colored crosses) for four codes in X-Z plane. The dashed lines show the bow shock (BS) and magnetopause (MP) from models by Slavin et al. (2009) for BS and Shue et al. (1997) for MP. The paraboloid of MP has parameters given by  $R_{ss} = 1.45 R_M$  and  $\alpha = 0.5$ , and parameters of BS model are  $p = 2.75 R_M$ ,  $\epsilon = 1.04$ , and  $X_0 = 0.5 R_M$ .

354

#### 4.2 MESSENGER case

355

356

357

358

359

360

361

362

363

364

365

366

367

368

369

370

371

372

373

374

In this section, we compare the simulation results with the magnetic field obtained by MESSENGER. Profiles of the three components of the magnetic field and its magnitude with the data from MESSENGER, and solar wind proton density and magnitude of velocity from four different models are shown in Figure 4. The profiles of four simulations are presented using colored lines, and MESSENGER magnetometer data is shown using a black plain line. MESSENGER data corresponds to measurements during orbit 1415 from 4:30 UT to 10:00 UT. During this period, the spacecraft entered the magnetosphere from the tail side from the southern hemisphere and exited on the dayside, crossing the bowshock and the magnetopause twice in its path. Four vertical lines indicate the shock locations for both inbound and outbound crossings of MESSENGER. The figure shows that all four codes produce results in close agreement with MESSENGER data, especially inbound orbit. On the other hand, non of 4 models reproduce neither the location of bowshock and magnetopause on the outbound orbit. This may be due to the variation of the solar wind during the one orbit despite the quiet orbit was selected as much as possible. And also, due to the limitation of the particle instrument and its orbit, velocity and density of solar wind are arbitrary taken. Changing those values may make the fitting of shock locations better. Interestingly, there are clear differences between MHDs and hybrids on the fourth panel of Figure 4 around 7:50. Two hybrid lines show agreement with the observations while both MHD show lower intensity of the magnetic field. This may be related to the ion kinetics.

375 Taking advantage of this virtual sampling, we also extract the particle data, pro-  
376 ton density and the velocity along the MESSENGER trajectory. Because of the kinetic  
377 effect of ions, the lines from hybrid models are a little bit busy. However, the density pro-  
378 files among four models show good agreement while the velocity profiles diverse more.  
379 Around 7:50 UT, the spacecraft is passing through the northern cusp and then moving  
380 towards the dayside region. At 8:10 UT, where you can see the peak signature in the den-  
381 sity panel, which shows the compressed magnetosheath. The velocity profile of AIKEF  
382 shows off-trend at 6:30 to 7:00 UT, where the density becomes very low, this may be due  
383 to the handling of vacuum region in hybrid code.

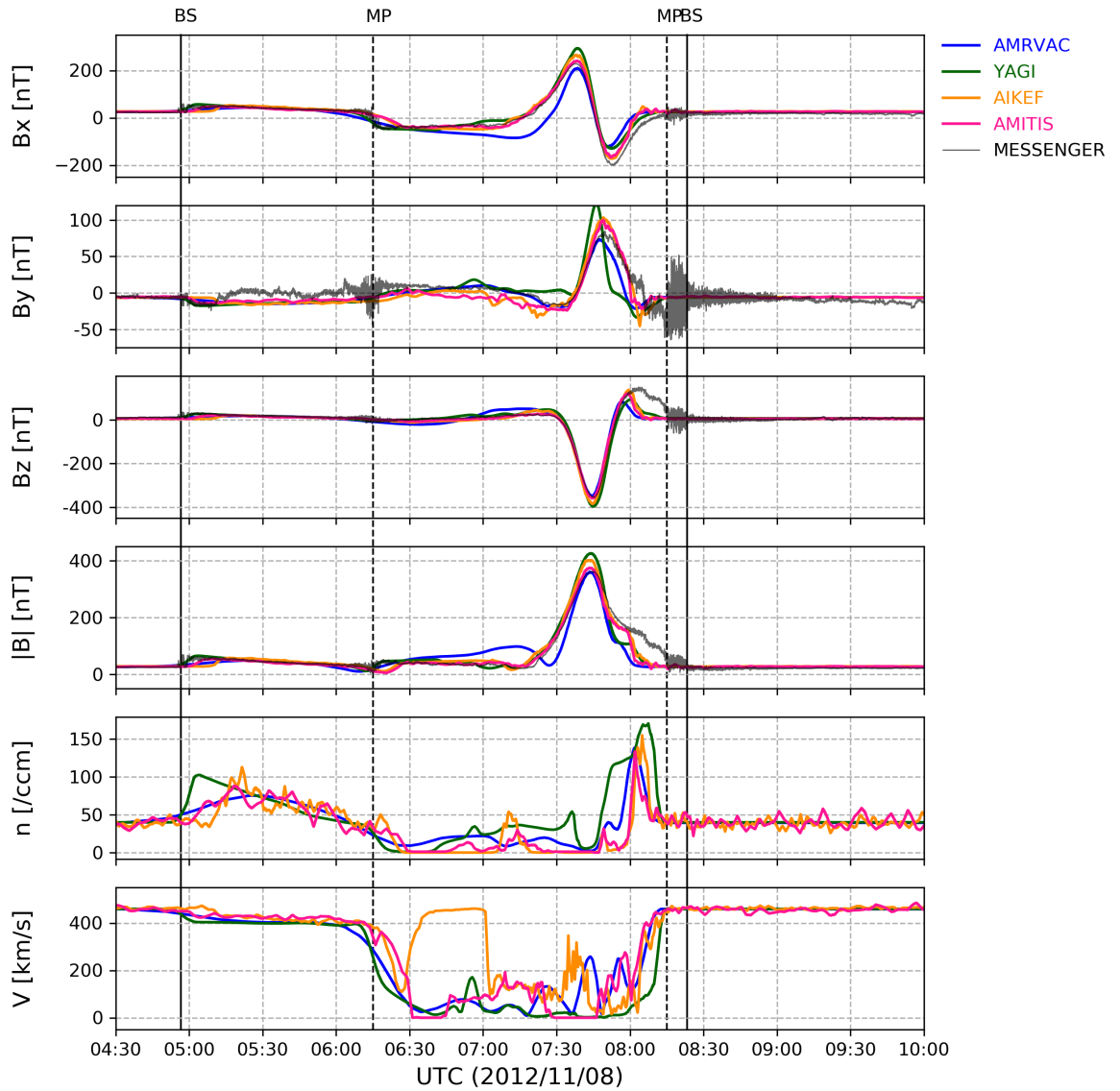


**Figure 4.** Magnetic field and particle data along orbit 1415 of the MESSENGER. Blue, green, orange, and red lines shows the results from AMRVAC, YAGI, AIKEF, AMITIS, respectively. The black line shows the magnetometer data from MESSENGER. Bow shock (BS) and Magnetopause (MP) crossings identified by observation are indicated using vertical solid and dashed line, respectively.

384

## 5 Discussion

385

386

387

388

389

390

391

392

393

394

395

396

397

398

399

400

401

402

403

404

405

406

407

408

409

410

411

412

413

414

415

416

417

418

419

420

Due to the limited particle instrument onboard MESSENGER and the single spacecraft, it is difficult to fit the locations of bowshock and magnetopause with models and observations. The solar wind varies in time in the real situation and there is no information about its velocity and density from the observation. It is necessary to assume those parameters so far. That's why it is normal that we do not have matched shock locations. However, in order to discuss more details, we derive the differences between magnetic field from observations and modelings (see Figure 5). Because the MESSENGER pass through the nightside region of the magnetosphere from 6:15 UT to 7:45 UT, the differences become larger so here we discuss only the differences around cusp and dayside region. Just before 5:00 UT, MESSENGER encounter the first bowshock crossing. Although all models show similar behaviors, the error time of this crossing is about 15 min. Then, while The z-component of magnetic field is well fit for all four models, y component is underestimated in four models. The first magnetopause crossing is fitted with some of models but models show more broad magnetopause crossing. At 7:50 UT where the MESSENGER moves from the nightside to the dayside in the northern hemisphere, two hybrids and two MHDs show similar behavior respectively. This is exactly after the cusp crossing and before entering the magnetosheath and the MESSENGER seems to be moving around the dayside magnetopause. Although our four models have small differences in the structure of the dayside magnetosphere, MESSENGER is along the magnetopause in MHDs while it is just inside the dayside magnetosphere in hybrids. It seems to be that hybrid models has magnetic pile-up in the dayside magnetosphere. According to Figure 2, MHD models show the similar profile inside magnetosphere as non-compressed one while the profiles of hybrids show more straight. It indicates that additional component, most probably the compression of magnetic field appears in hybrid, and this could be why MESSENGER in hybrids detects rather the higher magnetic field.

According to our results, some differences seen among multiple scale models seem to be rather due to the characteristics of each model, i.e., the numerical settings than the ion kinetics. The question that emerged here is : do we see any effects on the overview of the Hermean magnetosphere due to the ion kinetics?. One of those effects could be the dawn-dusk asymmetry. In general, the thickness of the magnetopause is different between on dusk and dawn due to the finite Larmor radius effect of ions, i.e., when the IMF is northward, the thickness of the magnetopause is going to be thicker on dawn and thinner on dusk. Since it is difficult to define the thickness of the magnetopause from our output, the thickness of the magnetosheath at the terminator has been compared. Of course no asymmetry could be observed in MHD, but in hybrids, we confirm that the thickness of the magnetosheath on dawn is 10 % thicker than that on dusk.

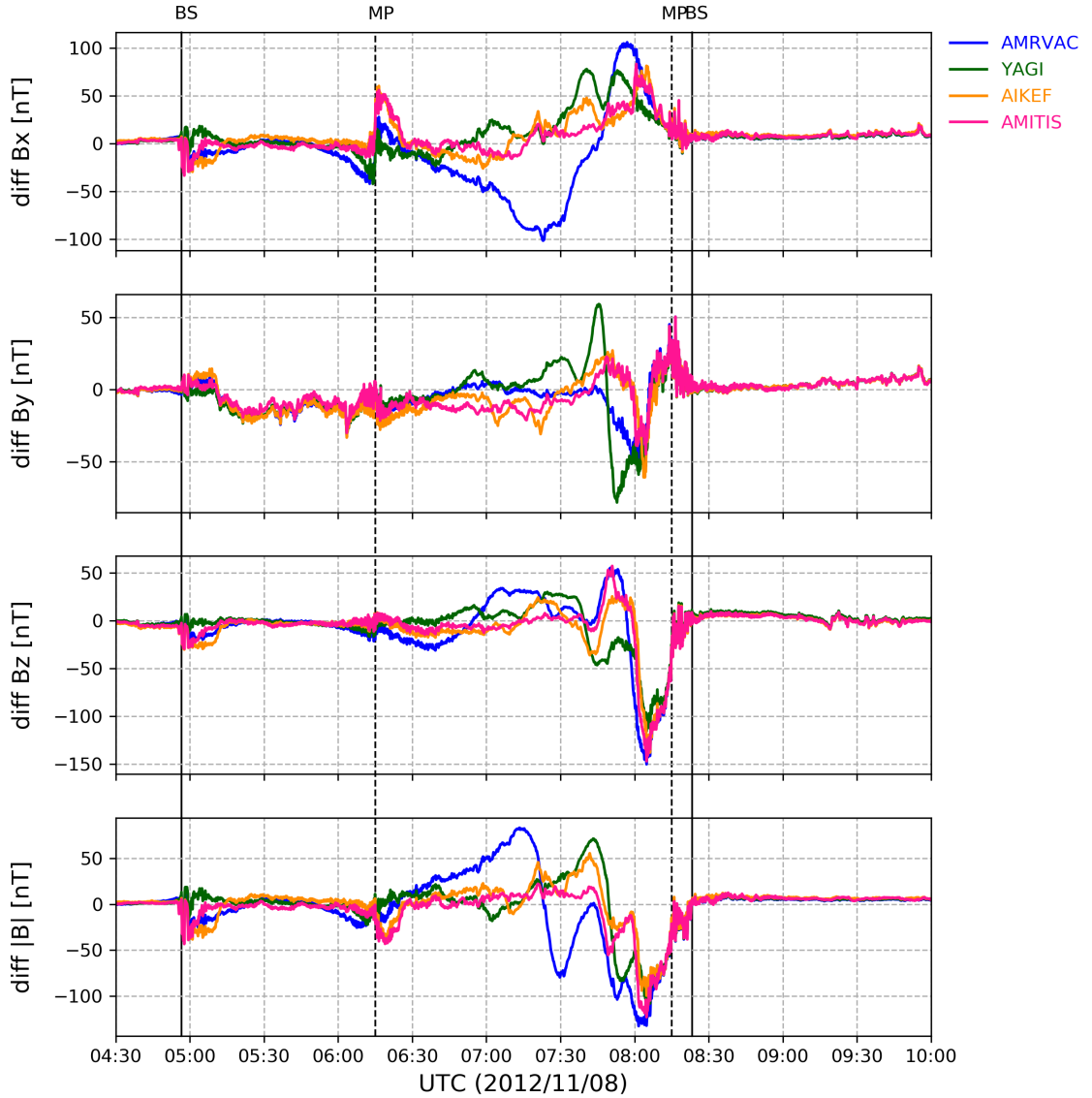


**Figure 5.** Subtraction between each model and MESSANGER observation of Magnetic field. and Blue, green, orange, and red lines shows the subtracted results from AMRVAC, YAGI, AIKEF, AMITIS, respectively. Bow shock (BS) and Magnetopause (MP) crossings identified by observation are indicated using vertical solid and dashed line, respectively.

421

### 5.1 Virtual sampling along Mio/MPO orbits

422

423

424

The aim of this SHOTS project is not only to compare the multiple codes and MESSANGER observation but also to prepare for the forthcoming BepiColombo observations by making a catalog of Mercury's magnetosphere under different solar wind conditions.



425 As the first step of this project, we employed four different MHD and hybrid codes. Fig-  
 426 ure 6 and 7 shows the virtual sampling of Mio and MPO during the nominal orbital phase  
 427 of BepiColombo with the input parameters of MESSENGER case. For an easy compar-  
 428 ison, the orbital plane is completely in  $x - z$  plane which corresponds to the orbit on  
 429 the 4th of April, 2026. In this period, both Mio and MPO moves inside the magneto-  
 430 sphere and collect all of plasma information around Mercury. In particular, plasma en-  
 431 vironment will be observed by the magnetometer onboard both Mio and MPO, MPPE  
 432 and PWI onboard Mio, SERENA onboard MPO .

433 In both Figure 6 and 7, the solid vertical lines show the crossing of southern and  
 434 northern terminators (indicated by T\_S and T\_N), and dashed vertical line shows the  
 435 point where the spacecraft crosses the subsolar point. In this case, Mio is moving along  
 436 the frontside magnetopause from 15:15 to 15:35, thus the enhancement of the magnetic  
 437 field intensity and velocity can be seen. The profiles close to the planet may change with  
 438 being closer to the planet due to the inner boundary condition at the surface or inside  
 439 the planet. Then Mio will move above the cusp region, and re-enter to the northern mag-  
 440 netosphere in the nightside. As you can see, after the crossing of northern terminator  
 441 at 15:50, the density and velocity profiles diverse more and more while the profile of mag-  
 442 netic field is still less varied. Those differences on the density and velocity are highly de-  
 443 pendent on the numerical settings such as a treatment of vacuum region in hybrid model,  
 444 the size of simulation domains.

445 On the other hand, MPO has a shorter orbital period and it passes through very  
 446 close to the planet. MPO is leaving from the southern magnetosphere in the nightside,  
 447 then cross the terminator, and enter the dayside magnetosphere. Just before 15:00, two  
 448 hybrids show the big bumping signatures in the density profile, indicating the cusp re-  
 449 gion (hatched by gray). Also, around 15:35, there are the small bumps again in the den-  
 450 sity profile, showing the trapped particles in the mid-night (represented by gray hatched  
 451 region). MPO's virtual sampling will be very useful to understand the structure and dy-  
 452 namics of the magnetosphere close to the planet. Overall, four models provide similar  
 453 virtual data along the orbit especially for the magnetic field. However, because of the  
 454 different models, we have different predictions for the timing of magnetopause crossing,  
 455 or of entering a certain region of the magnetosphere. From Mio's and MPO's virtual sam-  
 456 pling with various kinds of solar wind parameters and/or models, we are able to predict  
 457 the crossing of the cusp, the plasma sheet, or shocks with certain margins. Those mar-  
 458 gins contains the characteristics of model, or ion/electron kinetics. It should be stressed  
 459 here that the prediction from multiple-scale model would be necessary to maximize the  
 460 return of BepiColombo mission. In order to discuss more details with a Mio/MPO or-  
 461 bit, the simulation domain should be taken larger. In addition to those line profiles, vir-  
 462 tual sampling of energy-time spectrogram will be also provided in the near future. More-  
 463 over, not only those four MHDs and hybrids but also other codes will be soon employed  
 464 and discussed together. A number of questions raised here will be investigated with much  
 465 effort and work of the community, which will contribute to the detailed understanding  
 466 of solar wind interaction with Mercury's environment.

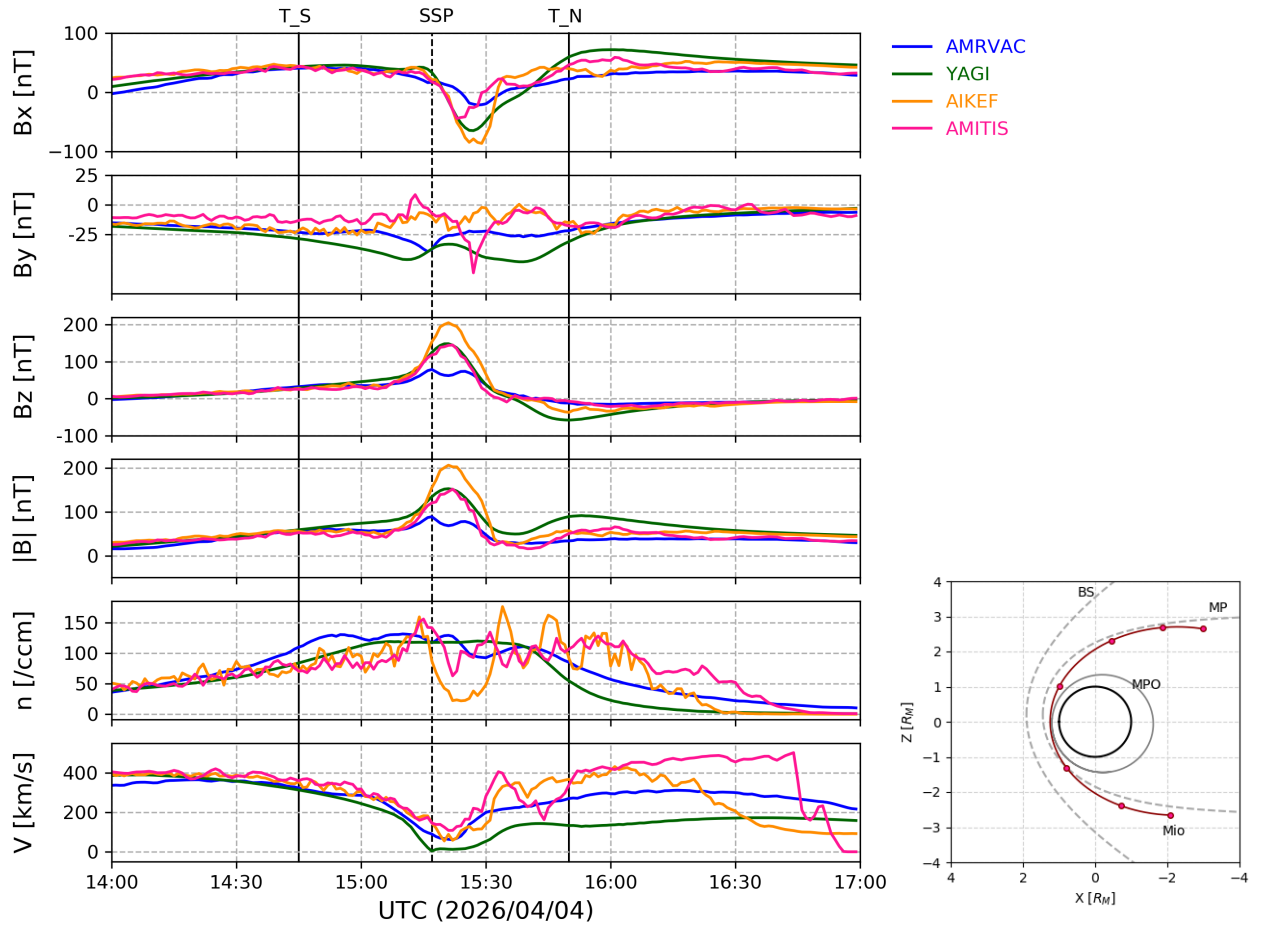


**Figure 6.** Magnetic field and particle data along the MIO orbit. The dots along the MIO orbit shows the position of MIO every 30 min. The figure format is same as Figure 4.

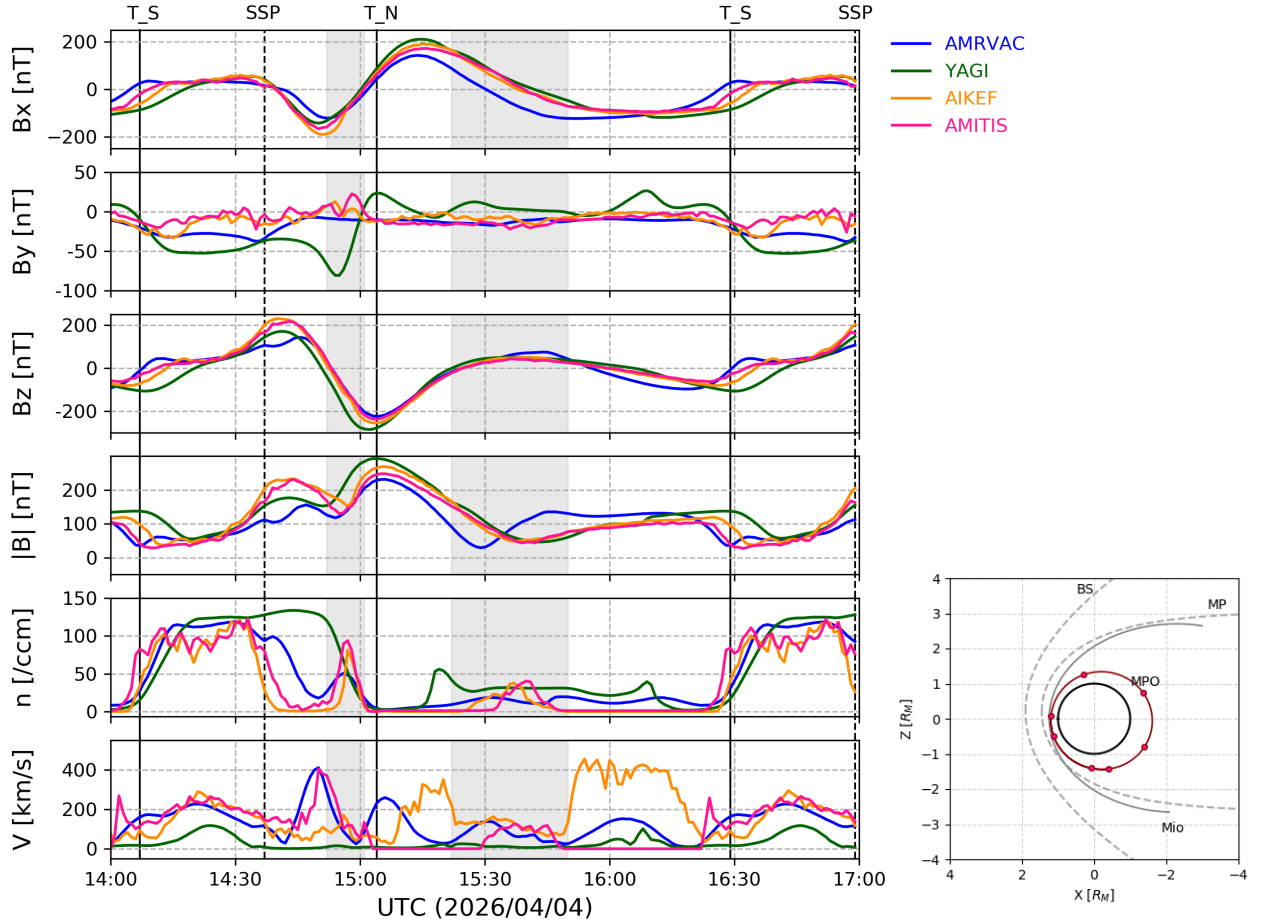


**Figure 7.** Magnetic field and particle data along the MPO orbit. The format is same as Figure 6. Two gray hatched regions indicate the cusp crossing and plasma sheet crossing.

## 6 Conclusions

Four different models run with the same input parameters of solar wind and results are stored in the same output format and compared by the common visualization tool. We found that, although all models show similar overview of the Hermean magnetosphere, the shock locations are highly affected by each numerical settings. However, the thickness of the magnetosheath in each model does not diverse. Generally, model comparison cannot remove any numerical effect which is also the characteristics of each model, however, we show that one clear result showing the effect of ion kinetics in hybrids is the dawn-dusk asymmetry. This classical comparison is useful to support the further development of each models, and also could be an assessment for the newly employed code in the future. In addition, the comparison with MESSENGER observation has also been conducted and confirmed that all four models are well developed and they show good agreement with observations. The further comparison with other orbits of MESSENGER will be conducted soon. One of SHOTS' purpose is to prepare the simulation catalog of the Hermean magnetosphere under different solar wind conditions and to work towards

482 maximizing the science return of the forthcoming BepiColombo observation using nu-  
 483 merical simulations. In this study, we have extracted the data from multiple models along  
 484 both Mio and MPO orbits and compared them for the first time. Those results could  
 485 be helpful when Mio/MPO start to obtain the data. The continuous project-based works  
 486 with community-wide effort will be very important not only for the nominal orbital phase  
 487 but also for the Mercury flybys.

## 488 Acknowledgments

489 The authors acknowledge support from the French space plasma physics data centre (Cen-  
 490 tre de Données de la Physique des Plasmas, CDPP: <http://www.cdpp.eu> funded by CNES  
 491 and CNRS). J.D. acknowledges support from NASA’s Solar System Exploration Research  
 492 Virtual Institute (SSERVI): Institute for Modeling Plasmas, Atmosphere, and Cosmic  
 493 Dust (IMPACT), and the NASA High-End Computing (HEC) Program through the NASA  
 494 Advanced Supercomputing (NAS) Division at Ames Research Center. All data neces-  
 495 sary to validate the findings presented in this manuscript can be found at [https://github](https://github.com/jandeca/Aizawa_etal_PSS_2020)  
 496 [.com/jandeca/Aizawa\\_etal\\_PSS\\_2020](https://github.com/jandeca/Aizawa_etal_PSS_2020) (DOI: XXX.XXX.XXX) in accordance with the  
 497 FAIR data project. The magnetometer data from MESSENGER observations is avail-  
 498 able in Planetary Data System.

## 499 References

- 500 Anderson, B. J., Slavin, J. A., Korth, H., Boardsen, S. A., Zurbuchen, T. H., Raines,  
 501 J. M., ... Solomon, S. C. (2011, December). The dayside magnetospheric  
 502 boundary layer at Mercury. *Planetary and Space Science*, *59*, 2037-2050. doi:  
 503 10.1016/j.pss.2011.01.010
- 504 Benna, M., Anderson, B. J., Baker, D. N., Boardsen, S. A., Gloeckler, G., Gold,  
 505 R. E., ... Zurbuchen, T. H. (2010, September). Modeling of the magneto-  
 506 sphere of Mercury at the time of the first MESSENGER flyby. *Icarus*, *209*,  
 507 3-10. doi: 10.1016/j.icarus.2009.11.036
- 508 Chen, Y., Toth, G., Jia, X., Slavin, J., Sun, W., Markidis, S., ... Raines, J. (2019).  
 509 Studying dawn-dusk asymmetries of mercury’s magnetotail using mhd-epic  
 510 simulations. *Journal of Geophysical Research: Space Physics (Submitted)*.
- 511 Dong, C., Wang, L., Hakim, A., Bhattacharjee, A., Slavin, J. A., DiBraccio, G. A.,  
 512 & Germaschewski, K. (2019, November). Global Ten-Moment Multifluid  
 513 Simulations of the Solar Wind Interaction with Mercury: From the Planetary  
 514 Conducting Core to the Dynamic Magnetosphere. *Geophys. Res. Lett.*, *46*(21),  
 515 11,584-11,596. doi: 10.1029/2019GL083180
- 516 Exner, W., Heyner, D., Liuzzo, L., Motschmann, U., Shiota, D., Kusano, K., &  
 517 Shibayama, T. (2018). Coronal mass ejection hits mercury: A.i.k.e.f. hybrid-  
 518 code results compared to messenger data. *Planetary and Space Science*, *153*,  
 519 89 - 99. Retrieved from [http://www.sciencedirect.com/science/article/](http://www.sciencedirect.com/science/article/pii/S0032063317303501)  
 520 [pii/S0032063317303501](http://www.sciencedirect.com/science/article/pii/S0032063317303501) doi: <https://doi.org/10.1016/j.pss.2017.12.016>
- 521 Fatemi, S., Poirier, N., Holmström, M., Lindkvist, J., Wieser, M., & Barabash, S.  
 522 (2018). A modelling approach to infer the solar wind dynamic pressure from  
 523 magnetic field observations inside Mercury’s magnetosphere. *A&A*, *614*, A132.  
 524 doi: 10.1051/0004-6361/201832764
- 525 Fatemi, S., & Poppe, A. R. (2018). Solar wind plasma interaction with asteroid 16  
 526 Psyche: implication for formation theories. *Geophys. Res. Lett.*, *45*(1).
- 527 Fatemi, S., Poppe, A. R., Delory, G. T., & Farrell, W. M. (2017). Amitis: A 3d  
 528 gpu-based hybrid-pic model for space and plasma physics. *Journal of Physics:*  
 529 *Conference Series*, *837*(1), 012017.
- 530 Fuqua Haviland, H., Poppe, A., Fatemi, S., Delory, G., & de Pater, I. (2019). Time-  
 531 Dependent Hybrid Plasma Simulations of Lunar Electromagnetic Induction in  
 532 the Solar Wind. *Geophys. Res. Lett.*, *46*(8), 4151–4160.

- 533 Garrick-Bethell, I., Poppe, A. R., & Fatemi, S. (2019). The Lunar Paleo-  
 534 Magnetosphere: Implications for the Accumulation of Polar Volatile Deposits.  
 535 *Geophys. Res. Lett.*, *46*(11), 5778-5787.
- 536 Génot, V., Beigbeder, L., Popescu, D., Dufourg, N., Gangloff, M., Bouchemit, M.,  
 537 ... Budnik, E. (2018, Jan). Science data visualization in planetary and helio-  
 538 spheric contexts with 3DView. *Planetary and Space Science*, *150*, 111-130. doi:  
 539 10.1016/j.pss.2017.07.007
- 540 Génot, V., Jacquy, C., Bouchemit, M., Gangloff, M., Fedorov, A., Lavraud, B., ...  
 541 Pinçon, J. L. (2010, May). Space Weather applications with CDDP/AMDA.  
 542 *Advances in Space Research*, *45*(9), 1145-1155. doi: 10.1016/j.asr.2009.11.010
- 543 Gershman, D. J., Zurbuchen, T. H., Fisk, L. A., Gilbert, J. A., Raines, J. M.,  
 544 Anderson, B. J., ... Solomon, S. C. (2012, Sep). Solar wind alpha parti-  
 545 cles and heavy ions in the inner heliosphere observed with MESSEN-  
 546 GER. *Journal of Geophysical Research (Space Physics)*, *117*, A00M02. doi:  
 547 10.1029/2012JA017829
- 548 Griton, L., Pantellini, F., & Meliani, Z. (2018). Three-dimensional magnetohydro-  
 549 dynamic simulations of the solar wind interaction with a hyperfast-rotating  
 550 uranus. *Journal of Geophysical Research: Space Physics*, *123*(7), 5394-5406.  
 551 Retrieved from [https://agupubs.onlinelibrary.wiley.com/doi/abs/](https://agupubs.onlinelibrary.wiley.com/doi/abs/10.1029/2018JA025331)  
 552 [10.1029/2018JA025331](https://agupubs.onlinelibrary.wiley.com/doi/abs/10.1029/2018JA025331) doi: 10.1029/2018JA025331
- 553 Jacquy, C., Génot, V., Budnik, E., Hitier, R., Bouchemit, M., Gangloff, M., ...  
 554 Pinçon, J. L. (2010, Jan). AMDA, Automated Multi-Dataset Analysis: A  
 555 Web-Based Service Provided by the CDDP. *Astrophysics and Space Science*  
 556 *Proceedings*, *11*, 239-247. doi: 10.1007/978-90-481-3499-1\_16
- 557 Jia, X., Slavin, J. A., Gombosi, T. I., Daldorff, L. K. S., Toth, G., & van der Holst,  
 558 B. (2015). Global mhd simulations of mercury's magnetosphere with coupled  
 559 planetary interior: Induction effect of the planetary conducting core on the  
 560 global interaction. *Journal of Geophysical Research: Space Physics*, *120*(6),  
 561 4763-4775. Retrieved from [https://agupubs.onlinelibrary.wiley.com/](https://agupubs.onlinelibrary.wiley.com/doi/abs/10.1002/2015JA021143)  
 562 [doi/abs/10.1002/2015JA021143](https://agupubs.onlinelibrary.wiley.com/doi/abs/10.1002/2015JA021143) doi: 10.1002/2015JA021143
- 563 Johnson, C. L., Philpott, L. C., Anderson, B. J., Korth, H., Hauck, S. A., Heyner,  
 564 D., ... Solomon, S. C. (2016, Mar). MESSENGER observations of induced  
 565 magnetic fields in Mercury's core. *Geophysical Research Letters*, *43*(6), 2436-  
 566 2444. doi: 10.1002/2015GL067370
- 567 Kabin, K., Gombosi, T., DeZeeuw, D., & Powell, K. (2000). Interaction of mercury  
 568 with the solar wind. *Icarus*, *143*(2), 397 - 406. doi: [http://dx.doi.org/10.1006/](http://dx.doi.org/10.1006/icar.1999.6252)  
 569 [icar.1999.6252](http://dx.doi.org/10.1006/icar.1999.6252)
- 570 Kallio, E., & Janhunen, P. (2003, November). Modelling the solar wind interac-  
 571 tion with Mercury by a quasi-neutral hybrid model. *Annales Geophysicae*, *21*,  
 572 2133-2145. doi: 10.5194/angeo-21-2133-2003
- 573 Kallio, E., Wurz, P., Killen, R., McKenna-Lawlor, S., Milillo, A., Mura, A., ... Jan-  
 574 hunen, P. (2008, Oct). On the impact of multiply charged heavy solar wind  
 575 ions on the surface of Mercury, the Moon and Ceres. *Planetary and Space*  
 576 *Science*, *56*(11), 1506-1516. doi: 10.1016/j.pss.2008.07.018
- 577 Keppens, R., Meliani, Z., van Marle, A. J., Delmont, P., Vlasis, A., & van der Holst,  
 578 B. (2012, Feb). Parallel, grid-adaptive approaches for relativistic hydro and  
 579 magnetohydrodynamics. *Journal of Computational Physics*, *231*(3), 718-744.  
 580 doi: 10.1016/j.jcp.2011.01.020
- 581 Korth, H., Anderson, B. J., Johnson, C. L., Slavin, J. A., Raines, J. M., & Zur-  
 582 buchen, T. H. (2018). Structure and configuration of mercury's magneto-  
 583 sphere. In S. C. Solomon, L. R. Nittler, & B. J. Anderson (Eds.), *Mercury:*  
 584 *The view after messenger* (chap. 16). Cambridge University Press.
- 585 Marsch, E., Schwenn, R., Rosenbauer, H., Muehlhaeuser, K. H., Pilipp, W., &  
 586 Neubauer, F. M. (1982, Jan). Solar wind protons: Three-dimensional ve-  
 587 locity distributions and derived plasma parameters measured between 0.3 and

- 588 1 AU. *J. Geophys. Res.*, *87*(A1), 52-72. doi: 10.1029/JA087iA01p00052
- 589 Milillo, A., Fujimoto, M., Kallio, E., Kameda, S., Leblanc, F., Narita, Y., ... Her-  
590 mean Environment WG members (2010, Jan). The BepiColombo mission: An  
591 outstanding tool for investigating the Hermean environment. *Planetary and*  
592 *Space Science*, *58*(1), 40-60. doi: 10.1016/j.pss.2008.06.005
- 593 Mukai, T., Yamakawa, H., Hayakawa, H., Kasaba, Y., & Ogawa, H. (2006). Present  
594 status of the bepicolombo/mercury magnetospheric orbiter. *Advances in Space*  
595 *Research*, *38*(4), 578 - 582. Retrieved from [http://www.sciencedirect.com/](http://www.sciencedirect.com/science/article/pii/S0273117705011579)  
596 [science/article/pii/S0273117705011579](http://www.sciencedirect.com/science/article/pii/S0273117705011579) (Mercury, Mars and Saturn) doi:  
597 <https://doi.org/10.1016/j.asr.2005.09.038>
- 598 Müller, J., Simon, S., Motschmann, U., Schüle, J., Glaßmeier, K.-H., & Pringle,  
599 G. J. (2011, 4). A.i.k.e.f.: Adaptive hybrid model for space plasma sim-  
600 ulations. *Computer Physics Communications*, *182*(4), 946-966. doi:  
601 10.1016/j.cpc.2010.12.033
- 602 Müller, J., Simon, S., Wang, Y.-C., Motschmann, U., Heyner, D., Schüle, J., ...  
603 Pringle, G. J. (2012, March). Origin of Mercury's double magnetopause:  
604 3D hybrid simulation study with A.I.K.E.F. *Icarus*, *218*, 666-687. doi:  
605 10.1016/j.icarus.2011.12.028
- 606 Müller, J., Simon, S., Wang, Y.-C., Motschmann, U., Heyner, D., Schüle, J., ...  
607 Pringle, G. J. (2012). Origin of mercury's double magnetopause: 3d hybrid  
608 simulation study with a.i.k.e.f. *Icarus*, *218*(1), 666 - 687. Retrieved from  
609 <http://www.sciencedirect.com/science/article/pii/S0019103512000164>  
610 doi: <https://doi.org/10.1016/j.icarus.2011.12.028>
- 611 Peng, I. B., Markidis, S., Laure, E., Johlander, A., Vaivads, A., Khotyaintsev, Y.,  
612 ... Lapenta, G. (2015). Kinetic structures of quasi-perpendicular shocks in  
613 global particle-in-cell simulations. *Physics of Plasmas*, *22*(9), 092109. doi:  
614 10.1063/1.4930212
- 615 Peng, I. B., Markidis, S., Vaivads, A., Vencels, J., Amaya, J., Divin, A., ... Lapenta,  
616 G. (2015). The formation of a magnetosphere with implicit particle-in-cell  
617 simulations. *Procedia Computer Science*, *51*, 1178 - 1187. (International Con-  
618 ference On Computational Science 2015: Computational Science at the Gates  
619 of Nature) doi: <http://dx.doi.org/10.1016/j.procs.2015.05.288>
- 620 Poppe, A. R. (2019). Comment on "The Dominant Role of Energetic Ions in So-  
621 lar Wind Interaction with the Moon" by Omid et al. *J. Geophys. Res.*, *124*(8),  
622 6927-6932.
- 623 Powell, K. G., Roe, P. L., Linde, T. J., Gombosi, T. I., & De Zeeuw, D. L.  
624 (1999, Sep). A Solution-Adaptive Upwind Scheme for Ideal Magnetohy-  
625 drodynamics. *Journal of Computational Physics*, *154*(2), 284-309. doi:  
626 10.1006/jcph.1999.6299
- 627 Raines, J. M., Gershman, D. J., Slavin, J. A., Zurbuchen, T. H., Korth, H., An-  
628 derson, B. J., & Solomon, S. C. (2014, Aug). Structure and dynamics of  
629 Mercury's magnetospheric cusp: MESSENGER measurements of protons and  
630 planetary ions. *Journal of Geophysical Research (Space Physics)*, *119*(8),  
631 6587-6602. doi: 10.1002/2014JA020120
- 632 Roberts, D. A., Thieman, J., Génot, V., King, T., Gangloff, M., Perry, C., ...  
633 Hess, S. (2018, Dec). The SPASE Data Model: A Metadata Standard  
634 for Registering, Finding, Accessing, and Using Heliophysics Data Obtained  
635 From Observations and Modeling. *Space Weather*, *16*(12), 1899-1911. doi:  
636 10.1029/2018SW002038
- 637 Sarantos, M., Reiff, P. H., Hill, T. W., Killen, R. M., & Urquhart, A. L. (2001, De-  
638 cember). A B<sub>x</sub>-interconnected magnetosphere model for Mercury. *Planetary*  
639 *and Space Science*, *49*(14-15), 1629-1635. doi: 10.1016/S0032-0633(01)00100  
640 -3
- 641 Slavin, J. A., Acuña, M. H., Anderson, B. J., Baker, D. N., Benna, M., Gloeckler,  
642 G., ... Zurbuchen, T. H. (2008, July). Mercury's Magnetosphere After MES-

- 643 SENDER's First Flyby. *Science*, *321*, 85-89. doi: 10.1126/science.1159040
- 644 Slavin, J. A., Baker, D. N., Gershman, D. J., Ho, G. C., Imber, S. M., Krimigis,  
645 S. M., & Sundberg, T. (2018). Mercury's dynamic magnetosphere. In  
646 S. C. Solomon, L. R. Nittler, & B. J. Anderson (Eds.), *Mercury: The view*  
647 *after messenger* (chap. 17). Cambridge University Press.
- 648 Slavin, J. A., Middleton, H. R., Raines, J. M., Jia, X., Zhong, J., Sun, W.-J., ...  
649 Mays, M. L. (2019). Messenger observations of disappearing dayside magne-  
650 tosphere events at mercury. *Journal of Geophysical Research: Space Physics*,  
651 *124*(8), 6613-6635. Retrieved from [https://agupubs.onlinelibrary.wiley](https://agupubs.onlinelibrary.wiley.com/doi/abs/10.1029/2019JA026892)  
652 [.com/doi/abs/10.1029/2019JA026892](https://agupubs.onlinelibrary.wiley.com/doi/abs/10.1029/2019JA026892) doi: 10.1029/2019JA026892
- 653 Trávníček, P., Hellinger, P., & Schriver, D. (2007, March). Structure of Mer-  
654 cury's magnetosphere for different pressure of the solar wind: Three dimen-  
655 sional hybrid simulations. *Geophysical Research Letters*, *34*, 5104. doi:  
656 10.1029/2006GL028518
- 657 Trávníček, P. M., Schriver, D., Hellinger, P., Herčík, D., Anderson, B. J., Sarantos,  
658 M., & Slavin, J. A. (2010). Mercury's magnetosphere: solar wind inter-  
659 action for northward and southward interplanetary magnetic field: Hybrid  
660 simulation results. *Icarus*, *209*(1), 11 - 22. doi: [http://dx.doi.org/10.1016/](http://dx.doi.org/10.1016/j.icarus.2010.01.008)  
661 [j.icarus.2010.01.008](http://dx.doi.org/10.1016/j.icarus.2010.01.008)
- 662 Wang, Y.-C., Mueller, J., Motschmann, U., & Ip, W.-H. (2010, September). A hy-  
663 brid simulation of Mercury's magnetosphere for the MESSENGER encounters  
664 in year 2008. *Icarus*, *209*, 46-52. doi: 10.1016/j.icarus.2010.05.020
- 665 Wilson, I., Lynn B., Stevens, M. L., Kasper, J. C., Klein, K. G., Maruca, B. A.,  
666 Bale, S. D., ... Salem, C. S. (2018, June). The Statistical Properties of Solar  
667 Wind Temperature Parameters Near 1 au. *The Astrophysical Journal Supplement*  
668 *Series*, *236*(2), 41. doi: 10.3847/1538-4365/aab71c
- 669 Winslow, R. M., Anderson, B. J., Johnson, C. L., Slavin, J. A., Korth, H., Purucker,  
670 M. E., ... Solomon, S. C. (2013, May). Mercury's magnetopause and bow  
671 shock from MESSENGER Magnetometer observations. *Journal of Geophysical*  
672 *Research (Space Physics)*, *118*(5), 2213-2227. doi: 10.1002/jgra.50237
- 673 Yagi, M., Seki, K., & Matsumoto, Y. (2009). Development of a magnetohydro-  
674 dynamic simulation code satisfying the solenoidal magnetic field condition.  
675 *Computer Physics Communications*, *180*(9), 1550 - 1557. Retrieved from  
676 <http://www.sciencedirect.com/science/article/pii/S0010465509001210>  
677 doi: <https://doi.org/10.1016/j.cpc.2009.04.010>
- 678 Yagi, M., Seki, K., Matsumoto, Y., Delcourt, D. C., & Leblanc, F. (2010). For-  
679 mation of a sodium ring in mercury's magnetosphere. *Journal of Geo-*  
680 *physical Research: Space Physics*, *115*(A10). Retrieved from [https://](https://agupubs.onlinelibrary.wiley.com/doi/abs/10.1029/2009JA015226)  
681 [agupubs.onlinelibrary.wiley.com/doi/abs/10.1029/2009JA015226](https://agupubs.onlinelibrary.wiley.com/doi/abs/10.1029/2009JA015226) doi:  
682 10.1029/2009JA015226